Nano Research

ISSN 1998-0124 CN 11-5974/O4
https://doi.org/10.26599/NR.2026.94908719

Research Article

Coalescence angle-driven 1T-to-1H phase transition in monolayer TaS_2

Zhiqiang Guo[1,2,3,§], Wenqiang Shen[4,5,§], Shipeng Lu[1,2], Xuchao Jia[1,2,3], Bingkai Yuan[6], Zixuan Li[1,7], Chenxu Wang[1], Yang Shi[1,8], Yekai Song[9], Junfeng Gao[4,5](✉), Shujie Tang[1,2](✉)

[1] National State Key Laboratory of Materials for Integrated Circuits, Shanghai Institute of Microsystem and Information Technology, Chinese Academy of Sciences, Shanghai 200050, China

[2] 2020 X-Lab, Shanghai Institute of Microsystem and Information Technology, Chinese Academy of Sciences, Shanghai 200050, China

[3] School of Physical Science and Technology, ShanghaiTech University, Shanghai 201210, China

[4] Key Laboratory of Materials Modification by Laser, Ion and Electron Beams (Dalian University of Technology), Ministry of Education, School of Physics, Dalian 116024, China

[5] Suzhou Laboratory, Suzhou 215123, China

[6] Suzhou Institute of Nano-Tech and Nano-Bionics (SINANO), Chinese Academy of Sciences (CAS), Suzhou 215123, China

[7] School of Physics, East China Normal University, Shanghai 200241, China

[8] University of Chinese Academy of Sciences, No. 1 Yanqihu East Rd, Huairou District, Beijing 101408, China

[9] Shandong Provincial Key Laboratory of Monocrystalline Silicon Semiconductor Materials and Technology, College of Chemistry and Chemical Engineering, Dezhou University, Dezhou 253023, China

[§] Zhiqiang Guo and Wenqiang Shen contributed equally to this work.

Nano Res., **Just Accepted Manuscript** • https://doi.org/10.26599/NR.2026.94908719

https://www.sciopen.com/journal/1998-0124 on Apr. 8, 2026

Research Article

Coalescence angle-driven 1T-to-1H phase transition in monolayer TaS_2

Zhiqiang Guo[1,2,3,§], Wenqiang Shen[4,5,§], Shipeng Lu[1,2], Xuchao Jia[1,2,3], Bingkai Yuan[6], Zixuan Li[1,7], Chenxu Wang[1], Yang Shi[1,8], Yekai Song[9], Junfeng Gao[4,5] ✉, and Shujie Tang[1,2] ✉

[1]*National State Key Laboratory of Materials for Integrated Circuits, Shanghai Institute of Microsystem and Information Technology, Chinese Academy of Sciences, Shanghai 200050, China*

[2]*2020 X-Lab, Shanghai Institute of Microsystem and Information Technology, Chinese Academy of Sciences, Shanghai 200050, China*

[3]*School of Physical Science and Technology, ShanghaiTech University, Shanghai 201210, China*

[4]*Key Laboratory of Materials Modification by Laser, Ion and Electron Beams (Dalian University of Technology), Ministry of Education, School of Physics, Dalian 116024, China*

[5]*Suzhou Laboratory, Suzhou 215123, China*

[6]*Suzhou Institute of Nano-Tech and Nano-Bionics (SINANO), Chinese Academy of Sciences (CAS), Suzhou 215123, China*

[7]*School of Physics, East China Normal University, Shanghai 200241, China*

[8]*University of Chinese Academy of Sciences, No. 1 Yanqihu East Rd, Huairou District, Beijing 101408, China*

[9]*Shandong Provincial Key Laboratory of Monocrystalline Silicon Semiconductor Materials and Technology, College of Chemistry and Chemical Engineering, Dezhou University, Dezhou 253023, China*

[§]*Zhiqiang Guo and Wenqiang Shen contributed equally to this work.*

Received: 21 January 2026; **Revised:** 21 March 2026; **Accepted:** 8 April 2026

✉ Address correspondence to Junfeng Gao, gaojf@dlut.edu.cn; Shujie Tang, tangsj@mail.sim.ac.cn

Cite this article: *Nano Research*, 2026, 19, 94908719 https://doi.org/10.26599/NR.2026.94908719

ABSTRACT: Atomic-layer-thick two-dimensional transition metal dichalcogenides (2D TMDs) exhibit unique electronic structures with versatile phase-dependent tunability. The structural transition between trigonal (T) and hexagonal (H) phases critically modulates their properties, yet the underlying microscopic mechanisms demand rigorous elucidation through integrated experimental and theoretical investigations. Herein, we demonstrate that domain coalescence angles during growth govern the phase transition efficiency from monolayer 1T-TaS_2 to 1H-TaS_2; when adjacent domains merge at 60°, atoms at the grain boundary naturally rearrange to form 1H-phase nuclei. Density functional theory (DFT) calculations reveal that charge asymmetry at domain boundaries drives the preferential unidirectional growth of the 1H phase from these nucleation sites. By employing rapid cooling (~550 K·min^{-1}) to shorten the time window for phase conversion, we successfully suppressed the 1T-to-1H phase transition and synthesized large-area monolayer 1T-TaS_2 (≥180 nm × 100 nm), reducing the post-coalescence H-phase formation ratio from 75% to 24%. This study comprehensively deciphers the microscopic mechanisms of the 1T-to-1H phase transition via coupled experiments and theory, which possesses generalizability to TMDC materials, provides a reliable phase modulation strategy, and expands the methodology for precise microscopic-scale phase engineering.

KEYWORDS: two-dimensional transition metal dichalcogenides (2D TMDs), TaS_2, coalescence angles, 1T-to-1H phase transition, grain boundary, phase engineering

1 Introduction

Phase engineering of two-dimensional transition-metal dichalcogenides (2D TMDs) has emerged as a core research frontier in condensed matter physics and advanced materials science, as the ability to tailor their crystallographic polymorphs—governed by distinct metal coordination environments—unlocks unprecedented electronic, optoelectronic, and catalytic functionalities [1-4]. The precise modulation of octahedral (1T) and trigonal-prismatic (1H) phase stability not only provides a unique platform for unraveling fundamental strongly correlated phenomena (e.g., charge density waves, Mott insulators)[5-10] but also holds revolutionary potential for advancing next-generation technologies, including ultra-low-power quantum devices, high-efficiency electrocatalysts, and flexible optoelectronic systems [11-14]. Recent breakthroughs in external stimuli-driven phase control—such as substrate-mediated charge transfer, strain engineering, electrostatic gating, and chalcogen chemical potential tuning—have validated the feasibility of reversible 1T/1H phase conversion and metastable phase stabilization, underscoring the pivotal role of phase engineering in breaking the performance bottlenecks of traditional 2D materials [15-18].

Among TMDs, 1T-TaS_2 stands out as a prototypical platform for investigating polymorphic phase transitions, owing to its strong electron–lattice coupling and rich charge-density-wave (CDW) phase diagram [19, 20]. To date, various approaches have been developed to tune the 1T/1H phase balance in TaS_2, such as post-growth thermal annealing, electric-field modulation, chemical doping, and interface/heterostructure engineering [17, 21-24]. Yet, these

methods predominantly treat phase conversion as a macroscopic or quasi-equilibrium process, providing limited insights into the nucleation and evolution of phases at the microscopic level during film growth—when domains continuously nucleate, expand, and coalesce [25-27]. This gap hinders the rational design of high-quality phase-controlled TMD films.

Elucidating the microkinetic origins of growth-associated 1T-to-1H phase transitions remains challenging for several interrelated reasons. First, phase conversion typically nucleates at domain boundaries formed during coalescence, and the transient nature of growth-stage phase transitions poses a formidable challenge for real-time atomic-scale characterization [17, 28-31]. Second, multiple intrinsic growth-related factors—including interfacial stress, chalcogen chemical potential, and electronic reconstruction at grain boundaries—often act synergistically, obscuring the identification of the dominant microscopic driving force.[1, 32] Consequently, despite extensive phenomenological observations, the key microkinetic parameters governing the efficiency and directionality of the 1T-to-1H transition during growth remain poorly understood [33, 34].

Herein, we address these challenges by combining statistical analysis of post-growth atomic-scale imaging with kinetic control of the growth process, focusing on domain coalescence during monolayer 1T-TaS_2 growth to unravel growth-coupled phase transition mechanisms. By statistically analyzing hundreds of STM images from ~80 samples, we establish a direct correlation between microkinetic phase transitions and domain coalescence angles, thereby overcoming the limitation of non-real-time observation in revealing intrinsic transition drivers. Our statistical results identify coalescence angle as a key regulator of 1T-to-1H transition efficiency: 60° antiparallel coalescence significantly enhances the probability of local atomic rearrangements that nucleate the 1H phase, whereas 0° parallel coalescence predominantly preserves the 1T structure—effectively decoupling the complex synergistic effects of multiple growth factors. To directly probe the kinetic nature of this transition, we implemented a rapid-cooling protocol (~550 $K \cdot min^{-1}$) that shortens the effective phase conversion time window, cutting off the energy supply for phase conversion, reducing post-coalescence 1T-to-1H formation, and enabling the synthesis of large-area monolayer 1T-TaS_2 (≥180 nm × 100 nm). Density functional theory (DFT) calculations—focused on grain-boundary energetics, charge redistribution, and diffusion barriers—confirm that grain boundary charge asymmetry drives preferential unidirectional 1H growth. Collectively, our results establish domain coalescence angle and rapid cooling as coupled microscopic controls over phase evolution. This work develops a novel microscale geometric modulation pathway for 2D TMD phase engineering, advancing the precise control of phase distribution and laying a foundation for high-performance TMD-based devices.

2 Results and discussion

Figure 1a shows atomic structures of 1T- and 1H-TaS_2 (Ta: brown; upper/lower S: yellow/green): 1T-TaS_2 has staggered S layers, while 1H-TaS_2 has overlapping S layers. Since growth temperature plays a critical role in the MBE growth of TMD materials[27], DFT calculations confirm 1T-TaS_2 thermodynamic stability at elevated temperatures (Figure 1b). However, large-area monolayer samples grown at 1073 K exclusively exhibit 1H phase (Figure 2e), contradicting theoretical predictions. Supporting Information Figure S1 illustrates 1T/1H structural differences and validates their coexistence via characterizations. To address this inconsistency, we monitored dynamic growth and coalescence evolution via STM.

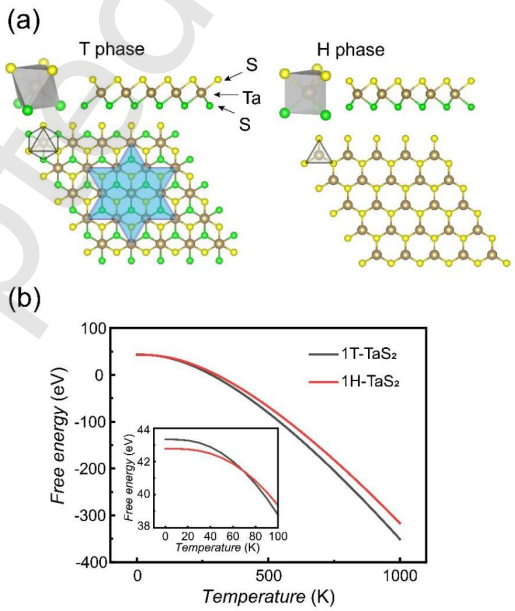

Figure 1 Phase transition during sample preparation. a. Atomic structures of 1T-TaS_2 (left) and 1H-TaS_2 (right): unit cell structure, side view, and top view (Ta: brown; upper/lower S: yellow/green; blue hexagram in 1T-TaS_2: CDW David star). b. DFT-calculated thermodynamic stability of 1T-TaS_2 and 1H-TaS_2 at different temperatures.

At 20 min of growth, high-density 1T nuclei (domain size ≤ 20 nm) dominate (coverage: 13%, nucleation fraction: 64%, Figure 2a). At 30 min, 1T domains grow to ~30 nm (coverage: 30%, nucleation fraction: 67%), with irregular 1H domains emerging in the lower left (Figure 2b). At 35 min, increased coalescence makes 1H dominant (coverage: 40%), while 1T coverage drops to 10% (nucleation fraction: 30%, Figure 2c). At 40 min, large-area 1H covers most regions (74%, Figure 2d), and nearly complete 1H coverage (85%, Figure 2e) is achieved at 70 min.

Total sample coverage increases with growth time, while 1T coverage and nucleation fraction first rise then fall, and 1H coverage increases sharply after 1T decline (Figure 2f: black = total, red = 1T, blue = 1H, green = 1T nucleation fraction). These results show that while elevated temperatures favor 1T nucleation, 1T-to-1H transition occurs during domain growth and coalescence, fully converting large-area monolayer samples to 1H phase.

After isolated domain coalescence, 1H dominates most regions with 1T retained only in partial corners. Previous work attributes this to denser atomic arrangement at edges/grain boundaries, promoting 1H transition for stress relief [35]. Stress-induced 1T transition and metallicity have also been reported[36, 37]. However, no phase transition was observed during STM scanning when tip-induced domain rotation/displacement causes coalescence. Although this concerns enhanced domain stability at low temperatures, we propose stress is not the primary driver for the transformation.

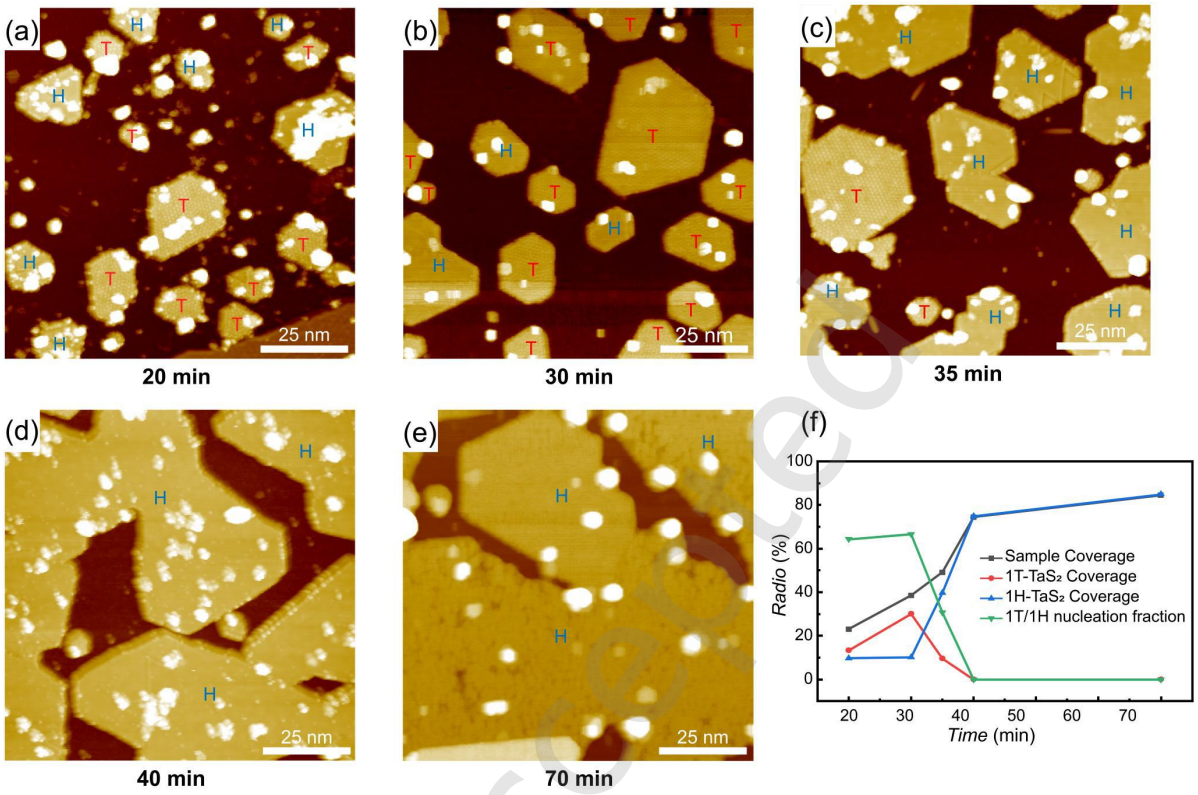

Figure 2. Phase transition during sample preparation. a–e. STM images after growth for 20, 30, 35, 40, and 70 min (scale bar: 25 nm): a. Initial 1T nuclei (≤20 nm, 64% nucleation fraction); b. 1T domains grow to ~30 nm with 1H domains emerging; c. Increased 1H domains from coalescence; d. Large-area 1H coverage (74%); e. Nearly complete 1H coverage (85%). In-situ continuous observation of the same spatial region during growth is not feasible due to technical limitations. These images are representative results from different samples prepared under identical growth conditions with varied growth durations, to demonstrate the evolution of domain nucleation, growth, coalescence and phase transition across different growth stages.f. Coverage (black: total; red: 1T-TaS_2; blue: 1H-TaS_2) and 1T nucleation fraction (green) during growth at 1073 K. Scan parameter: (a,c,d) Bias voltage V_B = −1 V, Tunneling current I_t = 50 pA; (b) V_B = −3 V, I_t = 100 pA; (b) V_B = −1 V, I_t = 30 pA.

To unravel the mechanism, we performed statistical analysis on the angle distribution between 1T-TaS_2 sample and substrate using hundreds of STM images from ~80 samples grown under different conditions. The dominant domain orientation is 0°, the normal angle distribution indicates weak domain-graphene substrate interactions, enabling easy domain rotation under external perturbations (Figure 3a). The angle distribution between adjacent 1T domain also shows a distinct pattern (Figure 3b). Using kernel smoothing in non-parametric regression, angles concentrate around 28° and 14° (not normal distribution), suggesting 1T-to-1H transition correlates with adjacent domain coalescence angle.

We defined the rotation angle between two coalescing domains as the "coalescence angle" (Figure 3c、Figure S2). Notably, parallel (0°) and antiparallel (60°) coalescence differ significantly even with edge overlap (Figure 3d). We analyzed coalescence angles before formation of observed irregular regions (Figure S3). While 1T-1H phase distribution of domain segments varies with coalescence angle, 0° and 60° show a clear distinction: 0° coalescence regions retain 1T phase (solid blue/red lines, Figure 3d), whereas 60° regions undergo 1T-to-1H transition (solid red/green lines).

Atomic models illustrate the mechanism (Ta atoms at grain boundaries marked in red): 0° coalescence maintains consistent upper/lower S positions around Ta atoms, enabling continuous 1T lattice formation (Figure 3e left, Figure 4a). 60° rotation of the right 1T domain causes S atom distribution mismatch: upper yellow S at 12 o'clock around left Ta vs. lower green S around right Ta. This triggers spontaneous grain boundary atomic rearrangement—staggered S layers overlap (1H hallmark)—forming 1H nuclei naturally (Figure 3d right, Figure 4b). These results confirm coalescence angle governs 1T-to-1H transition efficiency: 60° coalescence favors high-efficiency transition, while 0° coalescence inhibits transition and retains 1T phase.

Recently, studies on the T-to-H phase transition during $NbSe_2$ growth have suggested that this transition mechanism is a size effect controlled by edge energy, influenced by inter-sample collisions[17]. To clarify the relative importance of the domain size effect and coalescence angle effect in the 1T-to-1H phase transition of TaS_2, we

systematically analyzed the correlation between domain size, growth time and phase transition behavior based on our experimental results. The average domain size of 1T-TaS_2 is ≤20 nm after 20 min of growth, ~30 nm after 30 min of growth, and domains undergo massive coalescence with further size increase after 35 min of growth. Notably, the 1T-to-1H phase transition in our experiments mainly occurs after domain coalescence, rather than during the growth process of isolated domains. As shown in Figure 5c, large-size 1T domains can still maintain the 1T phase stably without phase transition, which directly confirms that domain size itself does not directly trigger the 1T-to-1H phase transition. We further compared the phase transition behavior of 0° and 60° coalesced domains in the same size range, and found that for 60° coalesced domains, the phase transition ratio is significantly higher than that of 0° coalesced domains in the same size interval, regardless of the domain size. Meanwhile, there is no obvious increasing trend of the phase transition ratio with the increase of domain size for both coalescence types.

Therefore, we conclude that the coalescence angle between adjacent domains is the dominant factor determining the efficiency of the 1T-to-1H phase transition, which has a more significant impact than the size effect. The phenomenon of increased 1H phase ratio in the late growth stage observed in our experiments is essentially caused by the significant increase of domain coalescence events in the late growth stage, rather than the phase transition induced by the increase of domain size.

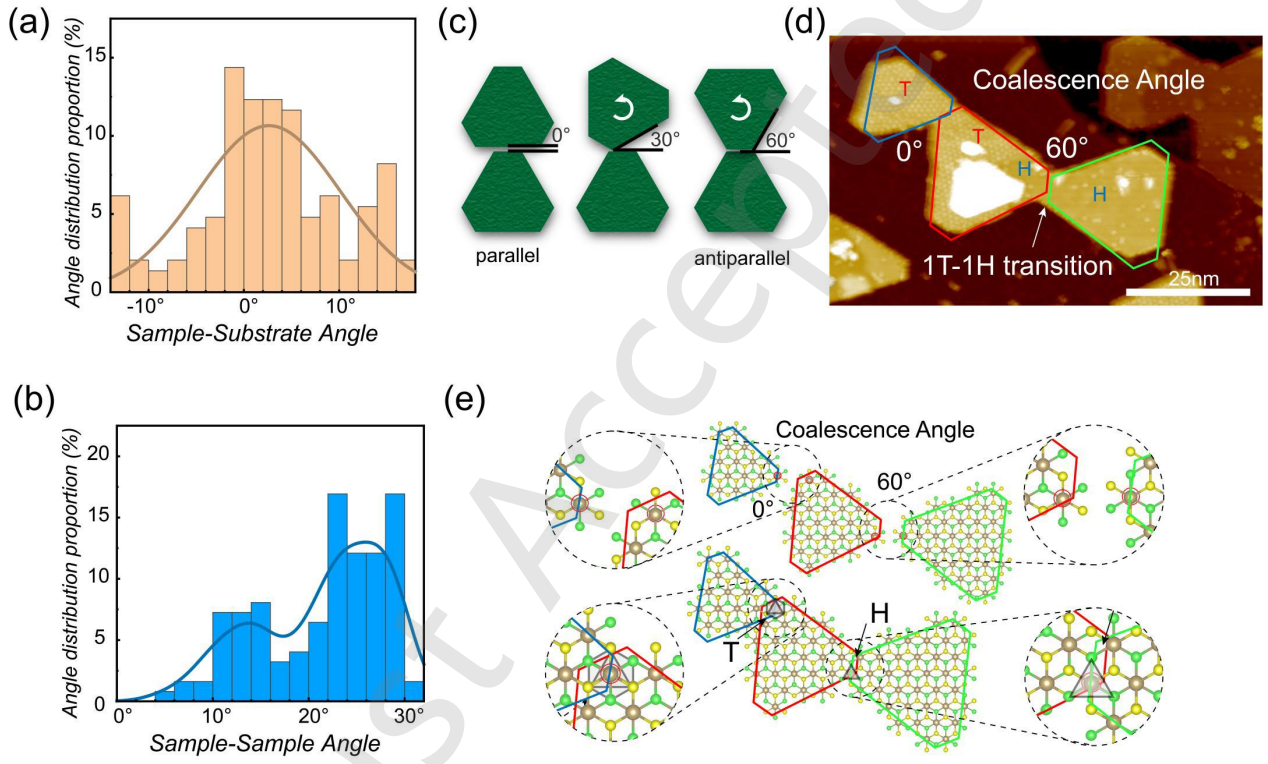

Figure 3. 1H-phase nucleus formation during 60° domain coalescence. a. Angle distribution between sample and substrate. b. Angle distribution between adjacent domain. c. Defines the rotation angle between two coalescing domains as the "coalescence angle". d. STM images of 0° and 60° coalescence (scale bar: 25 nm): 0° coalescence retains 1T phase (blue/red domains); 60° coalescence induces 1T-to-1H transition (green domain diffusing toward red domain). $V_B = -1$ V, $I_t = 10$ pA. e. Atomic structures of 0° and 60° coalescence: 0° maintains 1T phase (red-marked Ta overlap); 60° forms 1H nuclei via S layer overlap at the junction.

To further elucidate the diffusion behavior of the 1T-to-1H phase transition, we performed DFT calculations via the Nudged Elastic Band (NEB) method[38]. Periodic potential calculations show that the initial leftward 1H nucleus diffusion requires overcoming a 0.737 eV barrier, higher than subsequent diffusion barriers (Figure 4c).

Aperiodic potential calculations clarified complete diffusion kinetics: After initial 1H nucleus (H_0) formation at 60° grain boundaries, leftward diffusion forms H1 (0.567 eV barrier). From H_0 and H_1, further diffusion can proceed leftward (same direction) to form H_{2L} or rightward (opposite direction) to form H_{2R} (Figure 4d). The H_{2L} barrier (0.643 eV) is lower than H_{2R} (0.679 eV), indicating preferential unidirectional 1H diffusion (Figure 4e、Figure S5).

These computational results agree with experiments: in 60° coalescence regions, one grain boundary side is fully converted to 1H, while the other shows minimal diffusion (Figure 3e right). Coalescence-induced 1H grows continuously upon contact with 1T, eventually forming large-area 1H (Figures 2d–e).

The larger 1T lattice constant may induce interface curvature and energy fluctuations, with strain energy potentially reducing diffusion barriers. However, lattice

stretching/compression calculations show initial diffusion barriers of 1.137 eV and 1.347 eV, respectively (Figure S4)—much higher than previous values—tentatively excluding strain as a driver.

We propose unidirectional diffusion originates from grain boundary charge asymmetry post-1H nucleation. Bader charge analysis confirms this asymmetry drives preferential unidirectional 1H growth from 60° coalescence-induced nucleation sites[39]. S atoms carry negative net charges (higher absolute values indicate higher reactivity). After H0 formation (60° grain boundary), left S atoms have a higher net charge (0.828 |e|) than right S atoms (0.806 |e|), favoring leftward diffusion to form H1. Post-H1 formation, left S net charge (0.819 |e|) remains higher than right (0.813 |e|), promoting continuous leftward growth to H2L. The net charge difference (ΔS) decreases from 0.022 |e| to 0.006 |e|, stabilizing the system. In contrast, rightward diffusion to H2R increases ΔS to 0.019 |e| (left S: 0.821 |e|; right S: 0.802 |e|), reducing stability (Figure 4f).

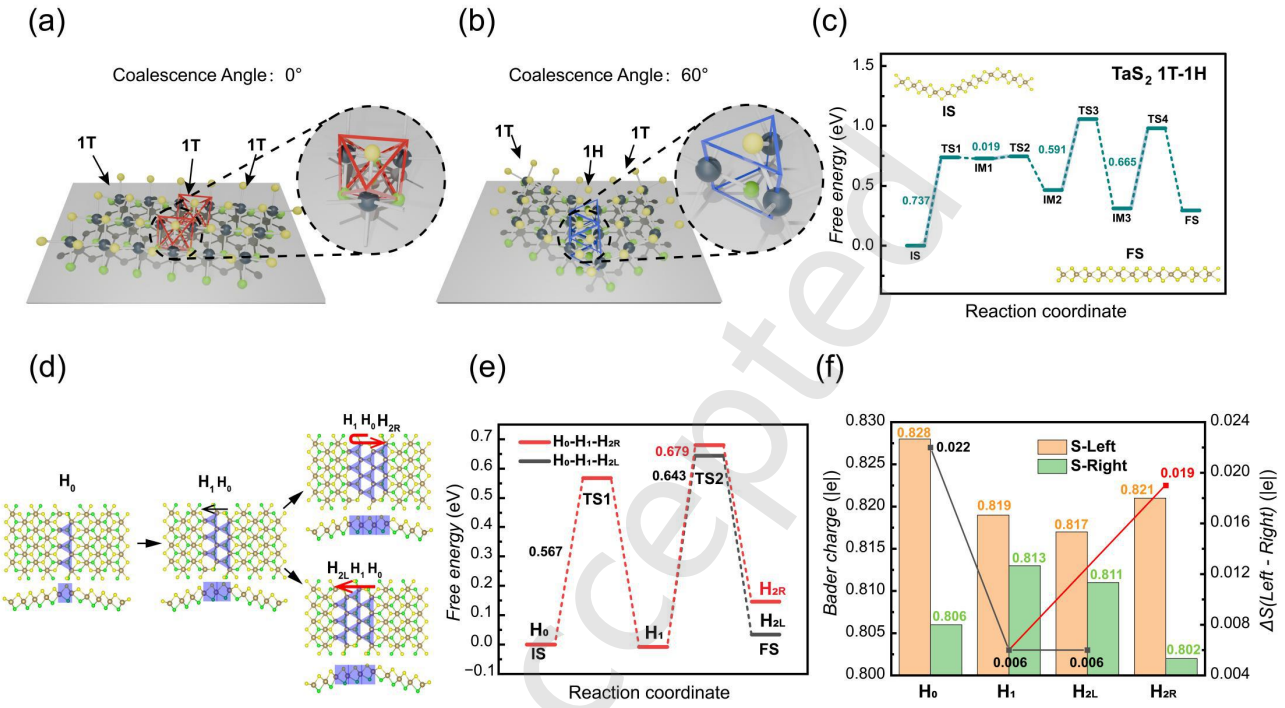

Figure 4. Kinetics of 1T-to-1H phase transition during 60° coalescence: preferential unidirectional 1H diffusion. a–b. Atomic models of 0° (octahedral 1T unit cells at junction) and 60° (trigonal prismatic 1H unit cells at junction) coalescence. c. Periodic potential calculations for leftward 1H nucleus diffusion (inset: initial/final atomic side views). d. Stepwise 1H diffusion: H_0 (initial nucleus) → H_1 (leftward) → H_{2L} (further leftward) or H_{2R} (rightward). e. Free energy of two diffusion paths (unidirectional diffusion is lower energy). f. Bader charges: left S atoms have higher net charge than right, favoring leftward diffusion; larger ΔS indicates stronger asymmetry.

The substrate effect of BLG on the 1T-to-1H phase transition was systematically investigated via formation energy calculation, differential charge density analysis and Bader charge analysis. (Figures S6-S7)The formation energy of 1T-TaS_2/BLG and 1H-TaS_2/BLG heterostructures are -0.022 eV/atom and 0.025 eV/atom, respectively. Bader charge analysis reveals a phase-selective doping effect, with average electron gain of Ta atoms being 1.2 |e| for 1T phase and 1.43 |e| for 1H phase, confirming that interfacial charge transfer from BLG to TaS_2 provides the electronic driving force for the phase transition. The lattice mismatch between TaS_2 and BLG is controlled below 3% to minimize interfacial stress effect.

DFT calculations confirm continuous 1H diffusion requires sustained energy input to overcome successive barriers (Figures 4c and 4e). Experimentally, despite higher 1T nucleation at elevated temperatures, slow cooling (5 $K \cdot min^{-1}$, black line in Figure 4b) to room temperature with the sample stage still forms large-area 1H domains, reducing 1T fraction. Residual substrate heat supplies diffusion energy and prolongs the phase conversion time window (period required for 1H diffusion/transition), facilitating unimpeded 1T-to-1H conversion[34, 40].

To suppress 1T-to-1H transition during annealing/cooling, we adopted rapid cooling (direct sample extraction post-growth, Figure 5a), increasing the cooling rate to 550 $K \cdot min^{-1}$ (Figure 5b red). This shortens the phase conversion time window and cuts off energy supply, enabling synthesis of large-area monolayer 1T-TaS_2 (≥180 nm × 100 nm) via multi-island coalescence (Figures 5c and S8).

60° coalescence domains in Figure 4c retain 1T phase, confirming rapid cooling effectively inhibits transition even for transition-susceptible 60° coalescence. Statistics (Figure 5d) quantify coalescence angle's regulatory effect: slow cooling yields 75% overall post-coalescence 1H formation rate (89% for 60°, 39% for 0°); rapid cooling reduces this to 24% (27% for 60°, 19% for 0°). These results validate

coalescence angle governs 1T-to-1H transition efficiency, which is effectively modifiable via rapid cooling.

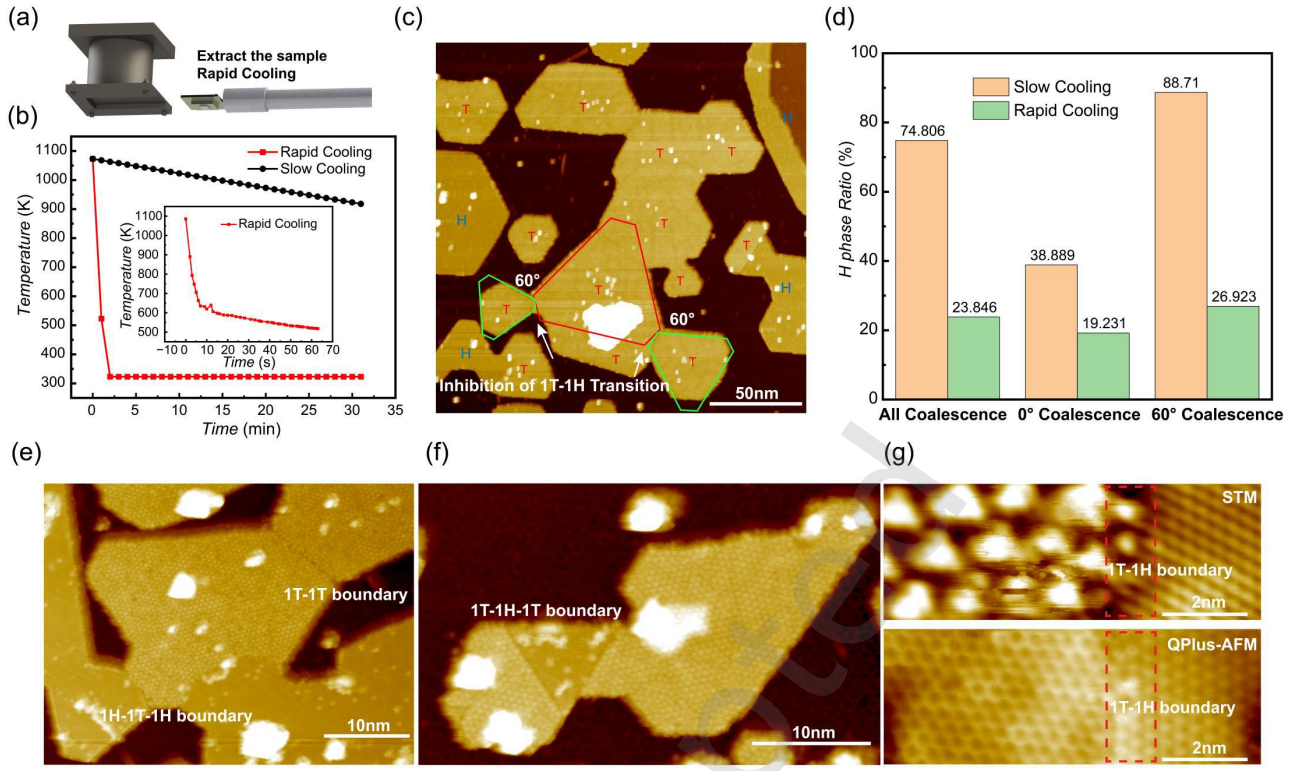

Figure 5. Inhibition of 1T-to-1H transition via rapid cooling. a. Schematic of rapid cooling (direct extraction from sample stage post-growth). b. Slow (black: 5 K·min^{-1}) and rapid (red: 550 K·min^{-1}) cooling rates (inset: rapid cooling temperature details). c. STM image post-rapid cooling (scale bar: 50 nm): large-area 1T-TaS_2 (≥180 nm × 100 nm) with 60° coalescence domains retaining 1T phase. d. Statistics of 1T-to-1H transition ratio: rapid cooling reduces post-coalescence 1H formation rate from 75% to 24% (60° coalescence: 89% → 27%). e. Different boundaries induced by rapid cooling (scale bar: left, middle, 10 nm; right, 2 nm). Scan parameter: (c,e,f) $V_B = -1$ V, $I_t = 10$ pA; (g) $V_B = -1$ V, $I_t = 40$ pA.

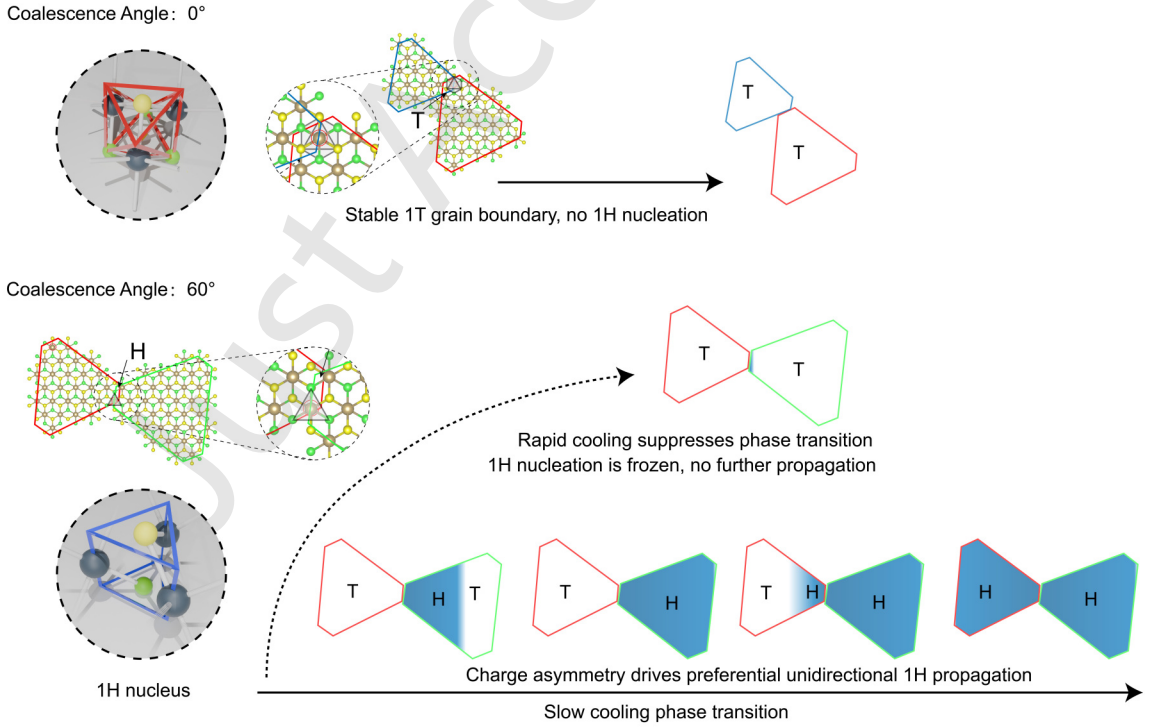

Figure 6. Schematic of the coalescence angle-dependent 1T-to-1H phase transition mechanism of monolayer TaS_2. 0° domain coalescence forms a stable 1T grain boundary with no phase transition, while 60° coalescence induces 1H nucleation at the grain boundary, followed by unidirectional 1H propagation under slow cooling; rapid cooling can effectively suppress the phase transition to retain the metastable 1T phase.

3 Conclusions

We systematically investigated phase coexistence and transition in monolayer 1T-TaS_2 growth, demonstrating that domain coalescence angles govern 1T-to-1H transition efficiency. Specifically, 60° domain merging triggers spontaneous grain boundary atomic rearrangement to form 1H nuclei, and grain boundary charge asymmetry drives preferential unidirectional 1H growth from these sites. Rapid cooling suppresses the transition by shortening the phase

conversion time window, enabling synthesis of large-area monolayer 1T-TaS_2 (≥180 nm × 100 nm) and regulating transition efficiency. This work precisely deciphers the microscopic mechanism of T-H phase transition through combined experimental and theoretical approaches, which possesses generalizability to TMDC materials. It deepens the understanding of phase dynamics in 2D transition metal dichalcogenides, provides a reliable phase transition modulation method, and expands the strategies for precise phase engineering regulation at the microscale, laying a foundation for high-performance TMD-based devices.

4 Mdthods

Bilayer Graphene (BLG) Substrate Fabrication: n-type SiC(0001) substrates were degassed at 600 °C for 2 h in a UHV chamber (base pressure: 1 × 10^{-8} mbar). BLG was synthesized via Nd:YAG laser heating (λ=1064 nm, pulse duration: 10 ns, repetition rate: 10 Hz): 1380 °C (1 min hold) → 600 °C (1 min hold), 60 cycles. RHEED (10 kV) confirmed BLG crystallinity (SI Figures 6).

Monolayer 1T-TaS_2 Growth via Molecular Beam Epitaxy (MBE): Monolayer 1T-TaS_2 was grown on BLG substrates via UHV MBE (base pressure: 6 × 10^{-9} mbar). A 2 mm-diameter Ta rod (99.999% purity, Alfa Aesar) was evaporated using an electron beam source with parameters: filament current 3.1–3.7 A, emission current 27–30 mA, acceleration voltage 2 kV, beam current 0.2–0.8 nA.

Sulfur (S) was supplied via a four-zone cracking furnace: high-purity S particles (purity: 99.999%) were heated to 70 °C to generate vapor, with valve and pipeline temperatures maintained at 200 °C and 400 °C, respectively, to prevent S condensation. S vapor was cracked at 1150 °C before introduction into the growth chamber, maintaining a chamber pressure of 1 × 10^{-7} mbar during growth (monitored via an ion gauge).

Key growth parameters: substrate temperature (550–800 °C, calibrated via an optical pyrometer) and growth time (30–120 min). Post-growth, samples were annealed in an S atmosphere (1 × 10^{-7} mbar) for 10 min at growth temperature, followed by two cooling protocols for phase control: slow cooling (5 °C/min on the sample stage) or two rapid cooling protocols with equivalent 1T-to-1H transition suppression efficiency (both ~30 °C/s cooling, sample cooled to room temperature within 1 min): (1) Ta and S sources shut off post-annealing, sample rapidly extracted to UHV once chamber vacuum fell below 5 × 10^{-8} mbar, then stored in a chamber with vacuum < 1 × 10^{-9} mbar; (2) only Ta source shut off, sample extracted under 1 × 10^{-7} mbar S atmosphere, S source shut off post-cooling, sample transferred to the same storage chamber after chamber vacuum dropped below 5 × 10^{-8} mbar.

Reflection High-Energy Electron Diffraction (RHEED): RHEED was used to monitor surface structure (filament current: 1.5 A; acceleration voltage: 10 kV).

Scanning Tunneling Microscopy (STM) and dI/dV Spectroscopy: STM measurements were conducted on a POLAR SPM system (Omicron, Germany) using home-made tungsten tips (electrochemical etching in KOH). All STM images were acquired at liquid helium temperature (4.4 K) with bias voltage (-1.0 V, applied to the sample) and tunneling current (10 pA–1 nA).

For phase evolution statistical analysis, STM images were collected via random, unbiased measurements on ~80 independently grown sample batches. Strict screening excluded frames with artifacts, contamination, substrate steps or multi-layer TaS_2; only images clearly resolving the 1T-phase CDW superlattice and 1H-phase lattice were retained, with hundreds of valid frames covering all growth and cooling conditions analyzed for statistical robustness. Phase coverage (target phase area / valid scanning area) and 1T nucleation fraction (intact 1T CDW domain count / total domain count) were quantified via polygon selection in SPIP software.

Domain crystallographic orientation and inter-domain coalescence angles were determined using the dominant CDW signal. FFT of high-resolution STM images was performed to extract CDW diffraction angles, with intrinsic lattice orientation obtained by correcting for the fixed 13.9° CDW-lattice misorientation; the coalescence angle was defined as the absolute lattice orientation difference between adjacent domains, cross-validated via a dashed frame matching method. Measurement uncertainty was ≤±1.5° (FFT) and ≤±3° (frame matching), negligible relative to the 0°–60° interval, with no impact on the statistical differentiation of the two characteristic coalescence angles.

DFT Calculations: All calculations are based on density functional theory (DFT) by the Vienna Ab initio Simulation Package (VASP), using the plane-wave basis with an energy cutoff of 450 eV (Figure S9), and the projector augmented wave pseudopotentials method. Generalized gradient approximation (GGA) with the Perdew–Burke–Ernzerhof (PBE) functional was used to describe the exchange–correlation functional. In addition, we applied the DFT-D3 (BJ) method to evaluate the van der Waals (vdW) effect in all of the calculations. All geometries are optimized using the convergence criteria of 10-5 eV for the electronic energy, and a conjugate-gradient algorithm was used to relax the ions until the force was less than 0.01 eV $Å^{-1}$. Phase diffusion was calculated by the climbing image nudged elastic band (CI-NEB) method with twelve images inserted to find transition states.

Two core structural models were constructed for targeted calculations: (1) A 1T|1H|1T superlattice grain boundary model, consisting of two 4-unit-cell 1T-TaS_2 nanoribbons with a 1-unit-cell 1H nucleus at the 60° coalescence boundary, S-terminated edges consistent with MBE-grown samples, a 15 Å out-of-plane vacuum layer, and periodic boundary conditions applied along both in-plane directions to eliminate spurious mirror interactions. (2) 1T/1H-TaS_2 and bilayer graphene heterostructure models, with 5 × 5 graphene/4 × 4 1H-TaS_2 and 4 × 4 graphene/3 × 3 1T-TaS_2 supercell matching schemes to minimize lattice mismatch, a 15 Å vacuum layer, and in-plane periodic boundary conditions. Brillouin zone sampling was performed with a k-point mesh at a reciprocal space density of 2π × 0.02 $Å^{-1}$ for all models.

The temperature-dependent free energy curves of 1T and 1H-TaS_2 (Figure 1b) were calculated under the harmonic approximation using the finite displacement method in Phonopy. A 3 × 3 × 1 supercell with a 0.01 Å finite displacement step was used to obtain the interatomic force constants and phonon density of states. The total Helmholtz free energy at each temperature (0–1000 K) was derived as $F(T) = E_0 + F_{vib}(T) - TS_{vib}(T)$, where E_0 is the 0 K DFT total energy, $F_{vib}(T)$ is the temperature-dependent vibrational free energy, and $TS_{vib}(T)$ is the lattice vibrational entropy, both calculated from the phonon density of states.

Acknowledgements

This work is supported by National Key R&D Program of China (Grants No. 2021YFA1401500), National Natural Science Foundation of China (No. 11974370), Chinese Academy of Sciences (No. JCPYJJ-2015), Autonomous deployment project of China National Key Laboratory of Materials for Integrated Circuits (No. NKLJC-Z2023-B03). The Strategic Priority Research Program of the Chinese Academy of Sciences (Grant No. XDB0670000).National Key R&D Program of China (Grants No. 2024YFA1409600), the National Natural Science Foundation of China (Grants No. 12374253, 22461160283), the research program from Suzhou Laboratory (SK-1502-2024-055) , the Fundamental Research Funds for the Central Universities （DUT24LK003）

Associated content

Supporting Information is available from the author.

Author contributions

Z.G. and W.S. contributed equally to this work. S.T. proposed and designed the research. Z.G. performed the MBE growth, carried out the STM measurements, and analyzed the data with help from S.L., X.J., Z.L., C.W., Y.S., and Y.S. B.Y. carried out the Q-Plus measurements. W.S. and J.G. carried out the density functional calculations and provided theoretical support. Z.G., W.S., J.G., and S.T. wrote the manuscript with contributions and comments from all authors.

Notes

The authors declare no competing financial interest.

Use of AI statement

During the preparation of this work, the authors used Doubao and ChatGPT in order to improve the linguistic fluency of the manuscript and assist in organizing the logical structure of the cover letter and discussion sections. After using this tool/service, the authors reviewed and edited the content as needed and take full responsibility for the content of the publication.

References

[1] Manzeli, S.;Ovchinnikov, D.;Pasquier, D.;Yazyev, O. V.; Kis, A. 2D transition metal dichalcogenides. *Nature Reviews Materials* **2017**, *2*, 17033.

[2] Kim, J. H.;Sung, H.; Lee, G.-H. Phase Engineering of Two‐Dimensional Transition Metal Dichalcogenides. *Small Science* **2024**, *4*, 2300093.

[3] Sajan, S.;Guo, H.;Agarwal, T.;Sánchez-Ramírez, I.;Patra, C.;Vergniory, M. G.;De Juan, F.;Singh, R. P.; M. Ugeda, M. Atomic-Scale Mapping of Superconductivity in the Incoherent CDW Mosaic Phase of a Transition Metal Dichalcogenide. *Nano Letters* **2025**, *25*, 6654-6660.

[4] Lee, J. S. H.;Sutter, T. M.;Karapetrov, G.;Musumeci, P.; Kogar, A. Observation of a hidden charge density wave liquid. *Nature Physics* **2025**, *22*.

[5] Rossnagel, K. On the origin of charge-density waves in select layered transition-metal dichalcogenides. *J Phys Condens Matter* **2011**, *23*, 213001.

[6] Yu, Y.;Yang, F.;Lu, X. F.;Yan, Y. J.;Cho, Y.-H.;Ma, L.;Niu, X.;Kim, S.;Son, Y.-W.;Feng, D.;Li, S.;Cheong, S.-W.;Chen, X. H.; Zhang, Y. Gate-tunable phase transitions in thin flakes of 1T-TaS_2. *Nature Nanotechnology* **2015**, *10*, 270-276.

[7] Zhang, Y.;Gao, Y.;Pulkkinen, A.;Guo, X.;Huang, J.;Guo, Y.;Yue, Z.;Oh, J. S.;Moon, A.;Oudah, M.;Gao, X.-J.;Marmodoro, A.;Fedorov, A.;Mo, S.-K.;Hashimoto, M.;Lu, D.;Rajapitamahuni, A.;Vescovo, E.;Kono, J.;Hallas, A. M.;Birgeneau, R. J.;Balicas, L.;Minár, J.;Hosur, P.;Law, K. T.;Morosan, E.; Yi, M. Kramers nodal lines in intercalated TaS_2 superconductors. *Nature Communications* **2025**, *16*.

[8] Wang, Y.;Li, Z.;Luo, X.;Gao, J.;Han, Y.;Jiang, J.;Tang, J.;Ju, H.;Li, T.;Lv, R.;Cui, S.;Yang, Y.;Sun, Y.;Zhu, J.;Gao, X.;Lu, W.;Sun, Z.;Xu, H.;Xiong, Y.; Cao, L. Dualistic insulator states in 1T-TaS_2 crystals. *Nature Communications* **2024**, *15*, 3425.

[9] Qiu, Z.;Han, Y.;Noori, K.;Chen, Z.;Kashchenko, M.;Lin, L.;Olsen, T.;Li, J.;Fang, H.;Lyu, P.;Telychko, M.;Gu, X.;Adam, S.;Quek, S. Y.;Rodin, A.;Castro Neto, A. H.;Novoselov, K. S.; Lu, J. Evidence for electron–hole crystals in a Mott insulator. *Nature Materials* **2024**, 10.1038/s41563-024-01910-3.

[10] Vaňo, V.;Amini, M.;Ganguli, S. C.;Chen, G.;Lado, J. L.;Kezilebieke, S.; Liljeroth, P. Artificial heavy fermions in a van der Waals heterostructure. *Nature* **2021**, *599*, 582-586.

[11] Voiry, D.;Fullon, R.;Yang, J.;Silva, D. C. C. E., Cecilia;Kappera, R.;Bozkurt, I.;Kaplan, D.;Lagos, M. J.;Batson, P. E.;Gupta, G.;Mohite, D., Aditya;Dong, L.;Er, D.;Shenoy, V. B.;Asefa, T.; Chhowalla, M. The role of electronic coupling between substrate and 2D MoS_2 nanosheets in electrocatalytic production of hydrogen. *Nature Materials* **2016**, *15*, 1003-1009.

[12] Wang, Q. H.;Kalantar-Zadeh, K.;Kis, A.;Coleman, J. N.; Strano, M. S. Electronics and optoelectronics of two-dimensional transition metal dichalcogenides. *Nature Nanotechnology* **2012**, *7*, 699-712.

[13] Chhowalla, M.;Shin, H. S.;Eda, G.;Li, L.-J.;Loh, K. P.; Zhang, H. The chemistry of two-dimensional layered transition metal dichalcogenide nanosheets. *Nature Chemistry* **2013**, *5*, 263-275.

[14] Chen, H.;Wang, F.-H.;Gao, Q.;Gao, X.-J.;Chen, Z.;Huang, Y.;Law, K. T.;Xu, X. Y.; Chen, P. Spectroscopic Evidence for Possible Quantum Spin Liquid Behavior in a Two-Dimensional Mott Insulator. *Physical Review Letters* **2025**, *134*, 066402.

[15] Cho, S.;Kim, S.;Kim, J. H.;Zhao, J.;Seok, J.;Keum, D. H.;Baik, J.;Choe, D. H.;Chang, K. J.;Suenaga, K.;Kim, S. W.;Lee, Y. H.; Yang, H. Phase patterning for ohmic homojunction contact in $MoTe_2$. *Science* **2015**, *349*, 625-628.

[16] Kang, K.;Xie, S.;Huang, L.;Han, Y.;Huang, P. Y.;Mak, K. F.;Kim, C.-J.;Muller, D.; Park, J. High-mobility three-atom-thick semiconducting films with wafer-scale homogeneity. *Nature* **2015**, *520*, 656-660.

[17] Liu, L.;Huang, X.;Huang, Z.;Li, P.;Song, X.;Wang, P.;Yang, H.;Zhang, Q.;Zhou, J.;Huang, Y.;Ding, F.;Gao, H. J.; Wang, Y. Islands Size‐Controlled Phase Transition in MBE‐Grown Two‐Dimensional $NbSe_2$. *Small* **2026**, *22*, e07950.

[18] Bang, J.;Lee, B.;Yang, H.;Kim, S.;Wulferding, D.; Cho, D. Charge-ordered phases in the hole-doped triangular Mott insulator 4Hb-TaS_2. *Physical Review B* **2024**, *109*.

[19] Wilson, J. A.;Di Salvo, F. J.; Mahajan, S. Charge-density waves and superlattices in the metallic layered transition metal dichalcogenides. *Advances in Physics* **1975**, *24*, 117-201.

[20] Darancet, P.;Millis, A. J.; Marianetti, C. A. Three-dimensional metallic and two-dimensional insulating behavior in octahedral tantalum dichalcogenides. *Physical Review B* **2014**, *90*.

[21] Li, L. J.;O'Farrell, E. C. T.;Loh, K. P.;Eda, G.;Özyilmaz, B.; Castro Neto, A. H. Controlling many-body states by the electric-field effect in a two-dimensional material. *Nature* **2016**, *529*, 185-189.

[22] Li, X.; Zhu, H. Two-dimensional MoS_2: Properties, preparation, and applications. *Journal of Materiomics* **2015**, *1*, 33-44.

[23] Zhang, W.;Gao, J.;Cheng, L.;Bu, K.;Wu, Z.;Fei, Y.;Zheng, Y.;Wang, L.;Li, F.;Luo, X.;Liu, Z.;Sun, Y.; Yin, Y. Visualizing the evolution from Mott insulator to Anderson insulator in Ti-doped 1T-TaS_2. *Npj Quantum Mater* **2022**, *7*.

[24] Zhang, W.;Ding, D.;Gao, J.;Bu, K.;Wu, Z.;Wang, L.;Li, F.;Wang, W.;Luo, X.;Lu, W.;Jin, C.;Sun, Y.; Yin, Y. Modulation of electronic state in copper-intercalated 1T-TaS_2. *Nano Research* **2022**, *15*, 4327-4333.

[25] Zhang, K. H.;Feng, S. M.;Wang, J. J.;Azcatl, A.;Lu, N.;Addou, R.;Wang, N.;Zhou, C. J.;Lerach, J.;Bojan, V.;Kim, M. J.;Chen, L. Q.;Wallace, R. M.;Terrones, M.;Zhu, J.; Robinson, J. A. Manganese Doping of Monolayer MoS_2: The Substrate Is Critical. *Nano Letters* **2015**, *15*, 6586-6591.

[26] Li, T.;Guo, W.;Ma, L.;Li, W.;Yu, Z.;Han, Z.;Gao, S.;Liu, L.;Fan, D.;Wang, Z.;Yang, Y.;Lin, W.;Luo, Z.;Chen, X.;Dai, N.;Tu, X.;Pan, D.;Yao, Y.;Wang, P.;Nie, Y.;Wang, J.;Shi, Y.; Wang, X. Epitaxial growth of wafer-scale molybdenum disulfide semiconductor single crystals on sapphire. *Nature Nanotechnology* **2021**, *16*, 1201-1207.

[27] Rajan, A.;Underwood, K.;Mazzola, F.; King, P. D. C. Morphology control of epitaxial monolayer transition metal dichalcogenides. *Physical Review Materials* **2020**, *4*.

[28] Bayer, B. C.;Kaindl, R.;Reza Ahmadpour Monazam, M.;Susi, T.;Kotakoski, J.;Gupta, T.;Eder, D.;Waldhauser, W.; Meyer, J. C. Atomic-Scale in Situ Observations of Crystallization and Restructuring Processes in Two-Dimensional MoS_2 Films. *ACS Nano* **2018**, *12*, 8758-8769.

[29] Zhu, X.;Wang, H.;Wang, K.; Xie, L. Progress on the in situ imaging of growth dynamics of two-dimensional materials. *Nanoscale* **2023**, *15*, 11746-11758.

[30] Skolimowski, J.;Gerasimenko, Y.; Žitko, R. Mottness collapse without metallization in the domain wall of the triangular-lattice Mott insulator 1T−TaS_2. *Physical Review Letters* **2019**, *122*, 036802.

[31] Kumar, P.;Horwath, J. P.;Foucher, A. C.;Price, C. C.;Acero, N.;Shenoy, V. B.;Stach, E. A.; Jariwala, D. Direct visualization of out-of-equilibrium structural transformations in atomically thin chalcogenides. *npj 2D Materials and Applications* **2020**, *4*.

[32] Wang, Y.;Cong, C.;Yang, W.;Shang, J.;Peimyoo, N.;Chen, Y.;Kang, J.;Wang, J.;Huang, W.; Yu, T. Strain-induced direct–indirect bandgap transition and phonon modulation in monolayer WS_2. *Nano Research* **2015**, *8*, 2562-2572.

[33] Lin, H.;Huang, W.;Zhao, K.;Qiao, S.;Liu, Z.;Wu, J.;Chen, X.; Ji, S.-H. Scanning tunneling spectroscopic study of monolayer 1T-TaS_2 and 1T-$TaSe_2$. *Nano Research* **2020**, *13*, 133-137.

[34] Zhang, Z.;Yang, P.;Hong, M.;Jiang, S.;Zhao, G.;Shi, J.;Xie, Q.; Zhang, Y. Recent progress in the controlled synthesis of 2D metallic transition metal dichalcogenides. *Nanotechnology* **2019**, *30*, 182002.

[35] Bu, K. L.;Zhang, W. H.;Fei, Y.;Wu, Z. X.;Zheng, Y.;Gao, J. J.;Luo, X.;Sun, Y. P.; Yin, Y. Possible strain induced Mott gap collapse in 1T-TaS_2. *Commun Phys-Uk* **2019**, *2*.

[36] Ma, L.;Ye, C.;Yu, Y.;Lu, X. F.;Niu, X.;Kim, S.;Feng, D.;Tománek, D.;Son, Y.-W.;Chen, X. H.; Zhang, Y. A metallic mosaic phase and the origin of Mott-insulating state in 1T-TaS_2. *Nature Communications* **2016**, *7*, 10956.

[37] Cho, D.;Cheon, S.;Kim, K. S.;Lee, S. H.;Cho, Y. H.;Cheong, S. W.; Yeom, H. W. Nanoscale manipulation of the Mott insulating state coupled to charge order in 1T-TaS_2. *Nat Commun* **2016**, *7*, 10453.

[38] Dong, J.;Ding, D.;Jin, C.;Liu, Y.; Ding, F. Edge Reconstruction-Dependent Growth Kinetics of MoS_2. *ACS Nano* **2022**, *17*, 127-136.

[39] Kumar, V.;Rajput, K.; Roy, D. R. Sensing applications of GeBi nanosheet for environmentally toxic/non-toxic gases: Insights

from density functional theory calculations. *Applied Surface Science* **2022**, *606*.

[40] Lin, H.;Huang, W.;Zhao, K.;Lian, C.;Duan, W.;Chen, X.; Ji, S.-H. Growth of atomically thick transition metal sulfide filmson graphene/6H-SiC(0001) by molecular beam epitaxy. *Nano Research* **2018**, *11*, 4722-4727.

Electronic Supplementary Material

Coalescence angle-driven 1T-to-1H phase transition in monolayer TaS_2

Zhiqiang Guo[1,2,3,§], Wenqiang Shen[4,5,§], Shipeng Lu[1,2], Xuchao Jia[1,2,3], Bingkai Yuan[6], Zixuan Li[1,7], Chenxu Wang[1], Yang Shi[1,8], Yekai Song[9], Junfeng Gao[4,5]✉, and Shujie Tang[1,2]✉

[1]*National State Key Laboratory of Materials for Integrated Circuits, Shanghai Institute of Microsystem and Information Technology, Chinese Academy of Sciences, Shanghai 200050, China*

[2]*2020 X-Lab, Shanghai Institute of Microsystem and Information Technology, Chinese Academy of Sciences, Shanghai 200050, China*

[3]*School of Physical Science and Technology, ShanghaiTech University, Shanghai 201210, China*

[4]*Key Laboratory of Materials Modification by Laser, Ion and Electron Beams (Dalian University of Technology), Ministry of Education, School of Physics, Dalian 116024, China*

[5]*Suzhou Laboratory, Suzhou 215123, China*

[6]*Suzhou Institute of Nano-Tech and Nano-Bionics (SINANO), Chinese Academy of Sciences (CAS), Suzhou 215123, China*

[7]*School of Physics, East China Normal University, Shanghai 200241, China*

[8]*University of Chinese Academy of Sciences, No. 1 Yanqihu East Rd, Huairou District, Beijing 101408, China*

[9]*Shandong Provincial Key Laboratory of Monocrystalline Silicon Semiconductor Materials and Technology, College of Chemistry and Chemical Engineering, Dezhou University, Dezhou 253023, China*

[§]*Zhiqiang Guo and Wenqiang Shen contributed equally to this work.*

✉Address correspondence to Junfeng Gao, gaojf@dlut.edu.cn; Shujie Tang, tangsj@mail.sim.ac.cn

Supporting information to https://doi.org/10.26599/NR.2026.94908719

Single-layer sample growth conditions

Figs. S1a–1d depict the side and top views of the atomic structures of 1T-TaS_2 and 1H-TaS_2. Ta atoms are represented by brown spheres, while S atoms in the upper and lower layers are denoted by yellow and green spheres, respectively. A distinct structural difference between these phases is observed in the stacking of the S layers: the upper and lower S layers are staggered in the 1T phase but overlapped in the 1H phase. All samples were synthesized on bilayer graphene (BLG). Monolayer samples exhibiting coexisting 1T-TaS_2 and 1H-TaS_2 phases were successfully fabricated at substrate temperatures maintained between 500 °C and 800 °C. As evidenced by the reflection high-energy electron diffraction (RHEED) pattern in Fig.S1f, the sharp streaky patterns corresponding to both the graphene substrate and the as-grown film confirm the high crystallinity of the monolayer sample and its incomplete coverage on the substrate.

Angle-resolved photoemission spectroscopy (ARPES) measurements provide additional evidence for phase coexistence (Fig.S1g). The metallic 1H-phase bands exhibit Fermi-level crossings, whereas the insulating 1T-phase flat bands are distinctly observed at approximately 0.2 eV below the Fermi level, consistent with the characteristic electronic structure of 1T-TaS_2. Scanning tunneling microscopy (STM) characterization was performed on samples synthesized at 600 °C for 30 minutes. As shown in Fig.S1i, high-quality monolayer 1T-TaS_2 with a lateral dimension of ~35 nm was successfully synthesized on the graphene substrate. At a measurement temperature of 4.4 K, the sample surface reveals periodic bright spots corresponding to the "Star of David" superstructure, formed by the contraction of thirteen Ta atoms (Fig.S1e). This structural motif constitutes a distinctive characteristic of the 1T-TaS_2 phase.

Notably, extending the growth time did not yield the desired large-area 1T-TaS_2. Instead, only small 1T-TaS_2 domains (~30 nm in size) were detected at the corners of the substrate or in the few-layer regions, while the large-area monolayer region was dominated by the 1H phase-indicating a spontaneous 1T-to-1H phase transition during growth. Although increasing the substrate temperature slightly enhanced the nucleation ratio of the 1T phase, attempts to fabricate large-area monolayer 1T-TaS_2 by further increasing the substrate temperature to 800 °C (to promote 1T nucleation) or reducing the Ta flux (to decrease nucleation density) were unsuccessful. Figs.S1j and S1k show the STM images of the 1T and 1H phases extracted from Fig.S1i, respectively, with their corresponding fast Fourier transform (FFT) patterns inserted as insets-providing crystallographic confirmation of each phase.

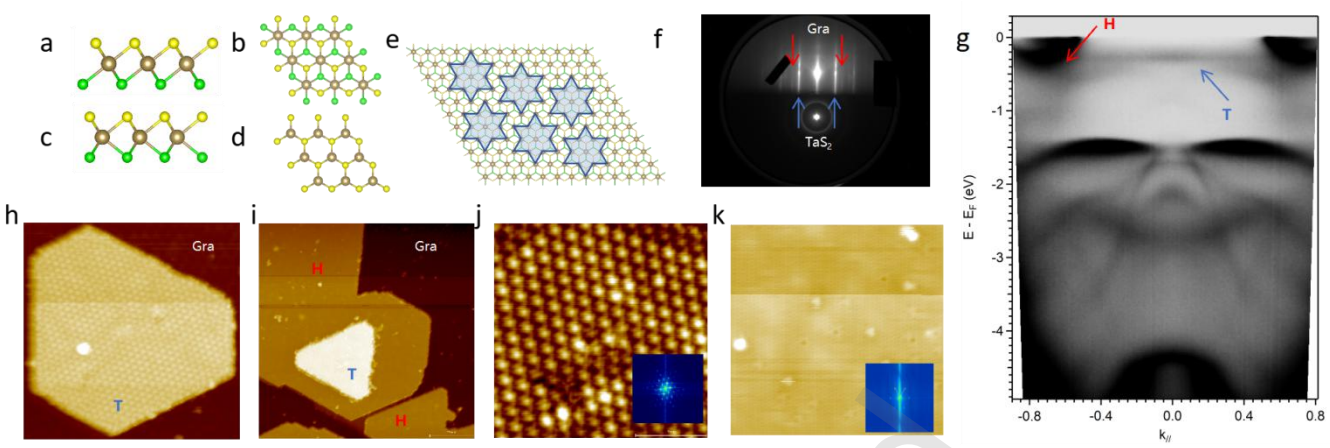

Figure S1: Phase coexistence and phase transition phenomena during sample preparation. a, b Side and top views of the atomic structure of 1T-TaS_2 , where brown spheres represent Ta atoms, and yellow and green spheres denote upper and lower S layers, respectively. c, d Side and top views of the atomic structure of 1H-TaS_2 , where brown spheres represent Ta atoms, and yellow and green spheres denote upper and lower S layers, respectively. e CDW in 1T-TaS_2 . f RHEED pattern of the sample. g ARPES result of the sample, showing coexistence of 1T and 1H phases. h Monolayer 1T phase grown at 600 °C for 30 min (scan range: 35.7 nm). i Large-area monolayer 1H phase with few-layer 1T phase grown at 600 °C for 40 min (scan range: 100 nm). j Atomic-resolution STM image of the 1T phase in Fig. 1i, where each bright spot corresponds to a "Star of David" (scan range: 15 nm); the inset shows the FFT pattern. k Atomic-resolution STM image of the 1H phase in Fig. 1i, where each spot represents a TaS_2 unit (scan range: 16 nm); the inset shows the FFT pattern.

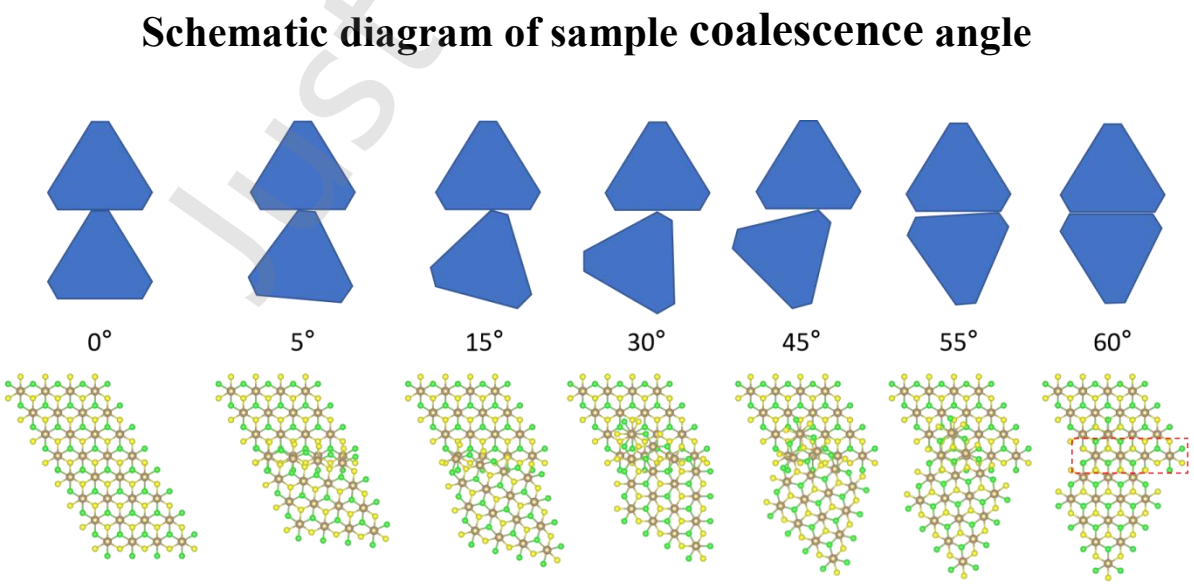

Figure S2: Sample coalescence angle and its atomic model.

Different coalescence scenarios observed during growth

In contrast, the coalescence angle between adjacent 1T domains plays a decisive role in the phase transition outcome. As illustrated in Fig. S2b, red solid circles denote the atomic configurations of Ta at the domain junction pre- and post-coalescence. When two 1T domains with identical crystal orientations collide (coalescence angle ≈ 0°), the stacking of upper and lower S layers around junction Ta atoms remains aligned. This uniform atomic arrangement facilitates the formation of a continuous 1T lattice at the junction. In stark contrast, when the right 1T domain is rotated by 60° (Fig. S2c), the stacking of S layers around junction Ta atoms (red solid circles) exhibits a mismatch: the left Ta atom has an upper-layer yellow S atom at the 12 o'clock position, whereas the right Ta atom has a lower-layer green S atom at the identical position. This mismatch induces the originally staggered S layers at the junction to undergo spontaneous overlap-a hallmark structural feature of the 1H phase. Thus, the coalescence of two 1T domains at a 60° angle induces the spontaneous formation of an 1H-phase nucleus at the junction.

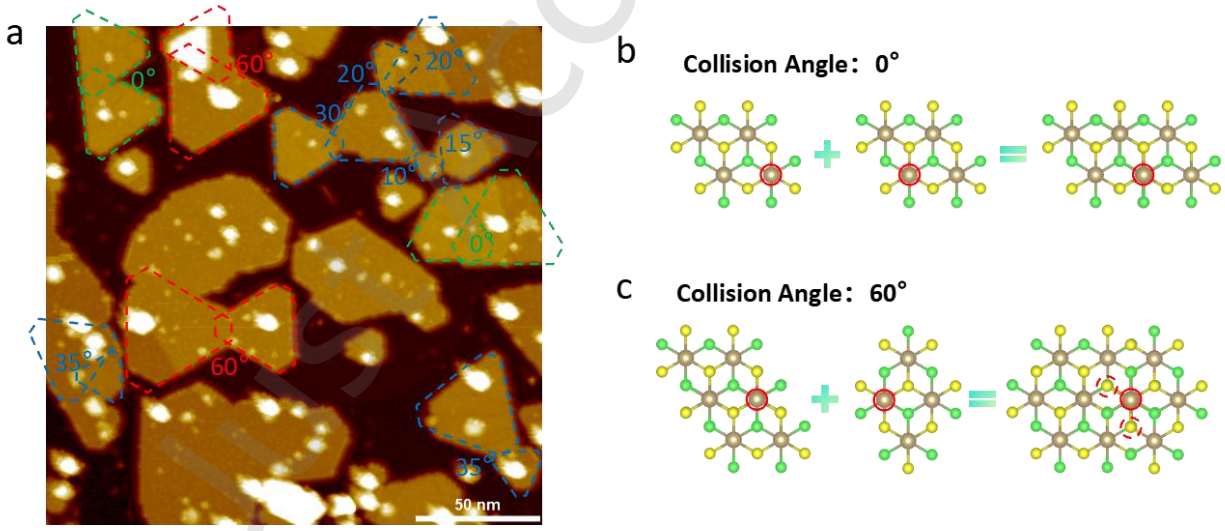

Figure S3 1T-1H Phase Transition Induced by Domain coalescence Angle. a 1T-1H phase transition on graphene. b Schematic of the atomic structure for 1T domains colliding at 0°: Ta atoms (marked by red circles) overlap, preserving the 1T phase. c Schematic of the atomic structure for 1T domains colliding at 60°: following the overlap of Ta atoms (marked by red circles), S atoms along the red dashed line vertically overlap, forming an 1H-phase nucleus.

Tensile and compressive calculation results

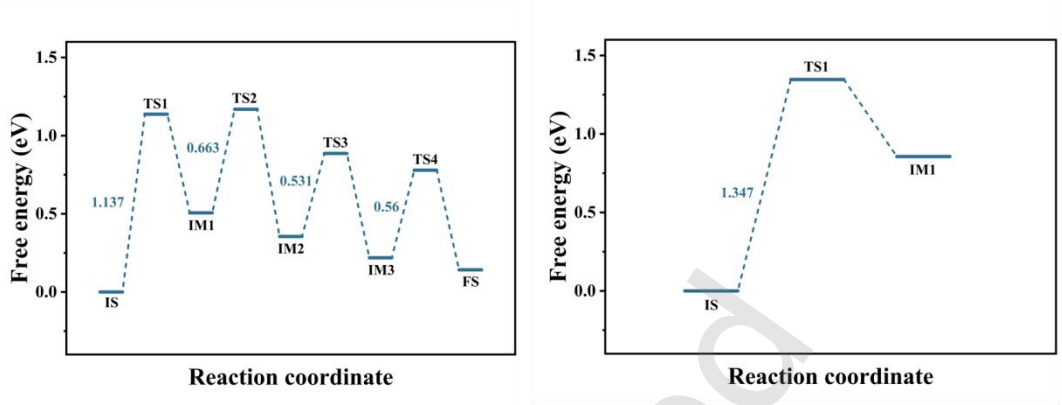

Figure S4: Energy barriers corresponding to 5% lattice stretching and compression. The height of the energy barrier is higher than the previous calculation results.

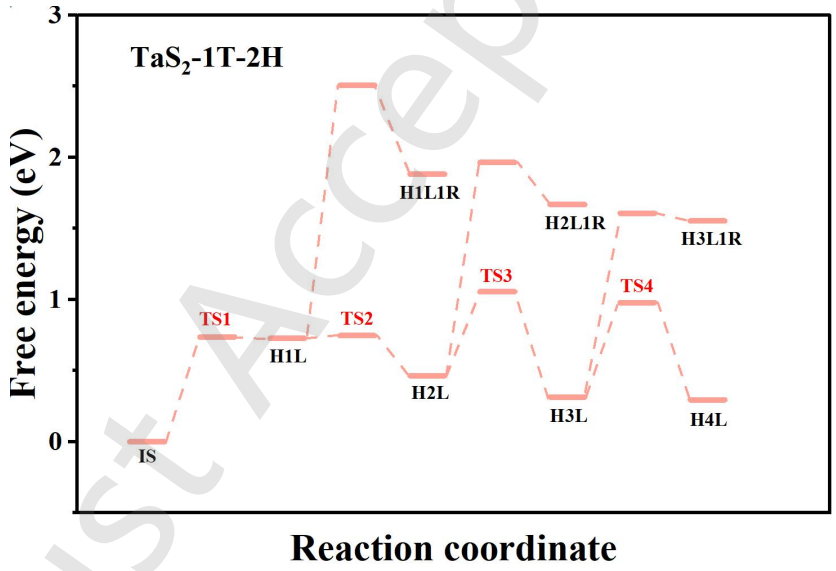

Figure S5: CI-NEB calculations of the long-range diffusion process of the 1H-phase nucleus.

We performed additional CI-NEB calculations for two types of diffusion processes: (1) forward long-range diffusion along the preferential direction, described as H(n)L→H(n+1)L (the 1H-phase nucleus expands one unit cell further to the left); (2) reverse diffusion along the opposite direction, described as H(n)L→H(n)L1R (the 1H-phase nucleus expands one unit cell to the right).

The calculation results show that the diffusion barrier of H1L→H2L is lower than that of H1L→H1L1R, the barrier of H2L→H3L is lower than that of H2L→H2L1R, and the barrier of H3L→H4L is lower than that of H3L→H3L1R. This is fully consistent with the trend of the previously reported H0→H1 and H1→H2

diffusion processes, where the diffusion barrier along the forward preferential direction is consistently significantly lower than that of the reverse diffusion. Further long-range diffusion calculations confirm that as the 1H-phase region expands, the forward diffusion barrier remains stable at 0.6–0.7 eV, while the reverse diffusion barrier is consistently higher, demonstrating that the driving force for unidirectional phase propagation is persistent during the entire phase transition process.

Based on these results, we conclude that reverse diffusion is not completely prohibited, but its higher kinetic barrier leads to a much slower diffusion rate than the forward unidirectional diffusion. On the time scale of our MBE growth experiments, only the preferential unidirectional growth of the 1H phase can be observed, which eventually leads to the complete conversion of the 1T phase on one side of the grain boundary to the 1H phase. This conclusion is in full agreement with our STM experimental observations.

Calculation results of differential charge

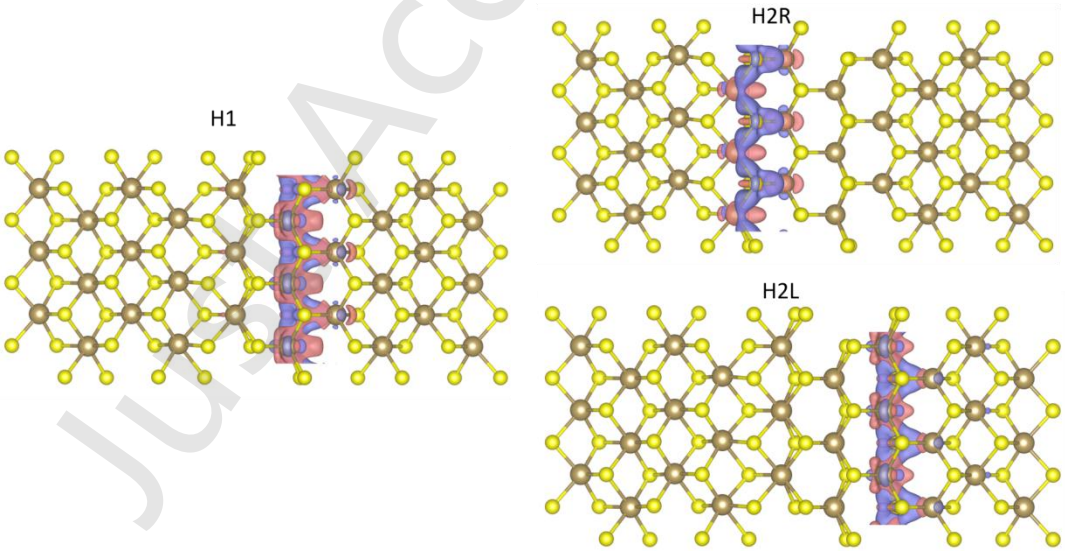

Figure S6: Differential charge calculation results.

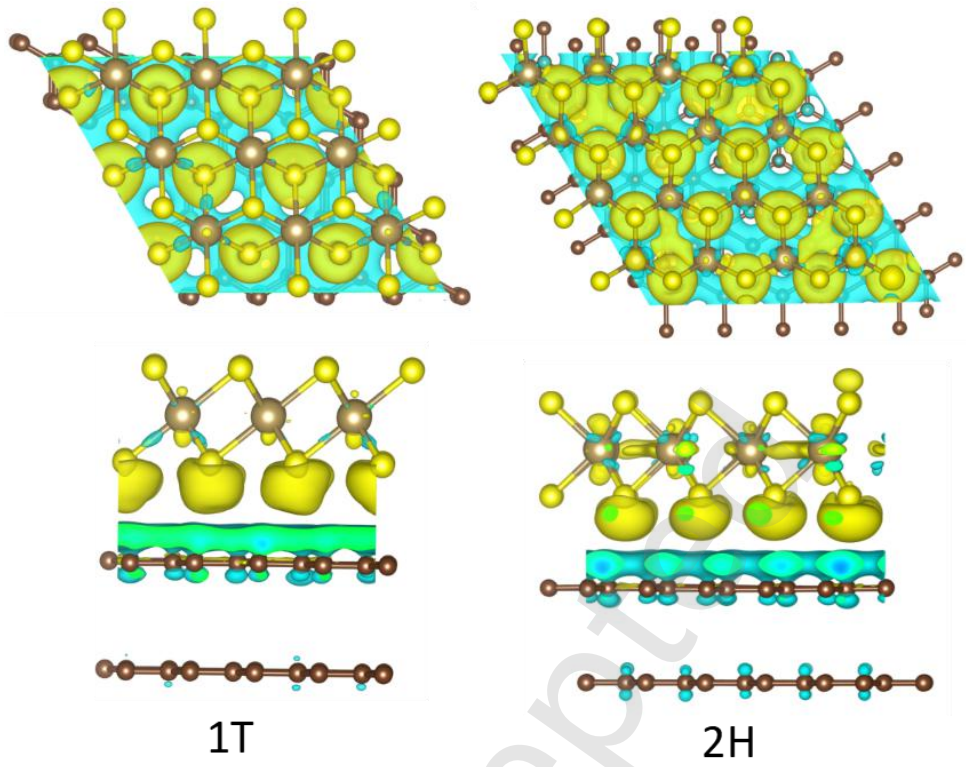

Figure S7: Energy transfer and charge transfer occur between double-layer graphene and TaS_2.

Large-area single-layer 1T-TaS2

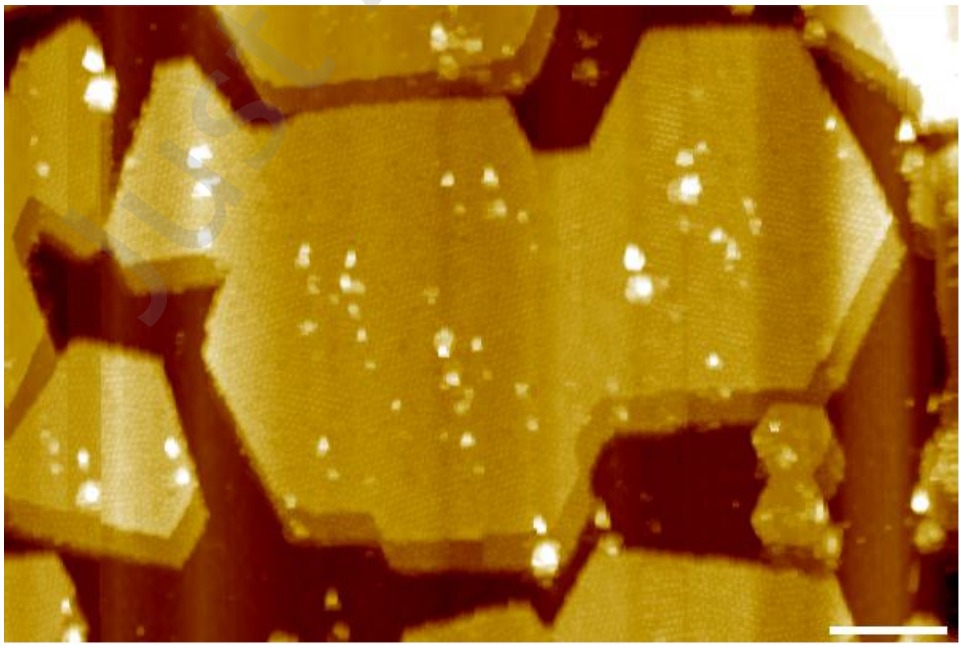

Figure S8 Large-area monolayer 1T-TaS2. STM image of a large-area monolayer 1T-TaS_2 .(scale bar: 25nm)

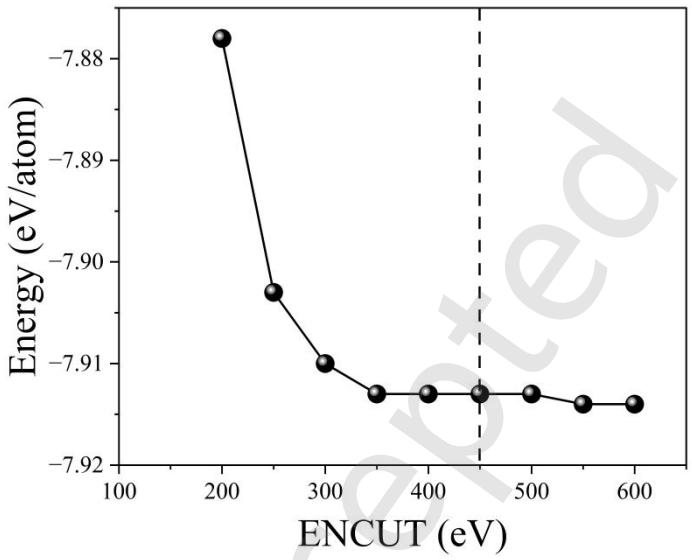

Figure S9 Cutoff-energy convergence tests.

We sincerely thank the reviewer for this constructive suggestion regarding the convergence of our DFT calculation parameters, which is critical to ensure the accuracy of our calculated diffusion barriers, especially given the relatively small differences between the reported diffusion barriers.

We have supplemented the plane-wave cutoff energy convergence test for our calculation system, with the test energy ranging from 200 eV to 600 eV at an interval of 50 eV. The test results show that when the cutoff energy reaches 400 eV, the change of the total energy of the system is less than 1 meV/atom, which fully meets the convergence requirement of high-precision first-principles calculations, and is sufficient to guarantee the accuracy of the calculated diffusion barriers in this work. We therefore selected 450 eV as the plane-wave cutoff energy for all calculations in this work, which ensures sufficient calculation accuracy while taking computational efficiency into account.

The relevant convergence test results have been supplemented into Figure Sx in the Supporting Information, and the corresponding citation and description have been added to the DFT Calculations subsection of the Methods section in the revised main text.